

Physics-based Models of Color and IR Video for Sensor Fusion

Sohail Nadimi and Bir Bhanu

Center for Research in Intelligent Systems

University of California, Riverside, California, 92521, USA

{sohail, bhanu}@cris.ucr.edu

Abstract

Physics based sensor fusion attempts to utilize the phenomenology of sensors to combine external conditions with data collected by the sensors into a global consistent dynamic representation. Although there have been a few approaches using this paradigm, it is still not entirely clear what kinds of physical models are appropriate for different sensing devices and conditions. We provide physical models that are suitable for the visible and infrared region of the spectrum. The physical models are described in detail. Moreover, the advantages and disadvantages of each model, their applicability, and guidelines for selecting the appropriate parameters are provided. Experimental results are also provided to indicate the applicability of the physical models.

Index terms: Dichromatic Reflection Model, Energy Equilibrium Model, Physics-based Fusion, Ward Reflection Model.

1. INTRODUCTION

Multisensor fusion attempts to combine the information from all available sensors into a unified representation. In other words, it refers to any stage in the integration process where there is an actual combination (or fusion) of different sources of sensory information into one representation. Some of the advantages to multisensor fusion are improved detection, increased accuracy, reduced ambiguity, robust operation, and extended coverage [1]. To illustrate how these advantages come about, relationship among sensors are categorized into three types of relations, complementary, competitive, and cooperative. Moreover, fusion can take place at pixel, feature or decision level. There has been an explosion of applications in multisensor fusion and integration; however, approaches utilized so far roughly fall into the following categories: statistical-based [2,3] (e.g., Bayesian, Dempster-Shafer, fuzzy, MAP, ML), AI-based [4,5] (e.g., Knowledge-based, rule-based, information theoretic), Algorithmic [6,7] (e.g., Graphs, Trees, Tables, and vote based techniques such as Hough transform), and Physics-based [8-10] (e.g., thermal, reflectance models). Statistical-based approaches have been used extensively at all levels of fusion due to their well-developed mathematics. They provide a unified framework and methods that can deal with sensor noise. These methods, however, require enormous amount of data and prior knowledge of statistical properties of the signals.

AI-based techniques have the advantage of incorporating external knowledge and heuristics that can be utilized to handle difficult applications. These methods, however, are more limited, domain specific and rely on heuristics provided by external experts. Algorithmic methods provide data structures that can be used to put the incoming data and information into a unified structure, where, sensory data can be treated in a unified manner. Well-developed algorithms such as graph search algorithms can then be applied. These methods are, therefore, suitable for cases where the data can be represented in the required format; moreover, once designed, they cannot be easily adapted if new types of sensors are introduced in the system.

Approaches that utilize the phenomenology of the sensor to model signal, based on the physical aspect of the world, fall under the category of physics-based fusion. Only recently, physics-based methods have found their way into the fusion domain. Unlike data driven approaches such as statistical and algorithmic methods, physics-based fusion does not require enormous amount of observations to be applicable. In a highly dynamic scenario where only a limited training set is available, physics-based methods can generate data based on physical models without having access to the actual data. External conditions along with sensory data can act on models which can react to these data to integrate all the sensory input into a dynamically global consistent representation. Some key features and advantages of physics-based fusion are: 1) Physical models can describe a scene based on sound models, which are mathematically proven; 2) It is natural and constructive to associate sensed signals to various physical parameters, which can serve as meaningful features; 3) the physical model provides known constraints that can be used to solve for the physical parameters; 4) The physical model can serve as an independent external information source, for example, conservation of energy is an absolute law; 5) It has enormous generalizing power and its prediction accuracy can increase with time; and 6) Physics-based fusion paradigm can be used in changing or evolving scenarios where the evolution of the scene can be modeled by physics.

2. PHYSICS-BASED FUSION AND RELATED APPROACHES

A physical model describes relation of object parameters (e.g., reflectance of surface, material density, surface

orientation, roughness, temperature, etc.) to scene parameters such as ambient temperature, direction of illumination, wind velocity, etc. The success of the physics-based approaches relies on how well the model can predict the phenomenon being investigated. This requires the sensing device to provide adequate accuracy and the model being general enough that can describe the scene within acceptable error. For these reasons, it has only been in the recent past that physics-based models have been incorporated into fusion models.

2.1 Related Approaches

An early work by Terzopoulos [9] introduced the concept of physically based deformable models whose physical behaviors are governed by the continuum mechanical equations of deformable bodies. The model has been applied to image contour extraction, stereo and motion matching and visual surface reconstruction. Pavlidis et al. [10] have developed an automatic passenger counting system based on sub-bands below SWIR. They perform fusion, by first splitting the NIR band into 1.1 - 1.4 μm and 1.4 - 1.7 μm then subtracting them from each other. This is chosen due to the fact that emittance detected by human skin abruptly changes (sharply drops) at 1.4 μm . In [8] a physical model based on the energy equilibrium is developed to model the thermal signal to segment an image. The fusion is viewed as the problem of relating scene parameters to object parameters. Since IR bands above 3 μm measure thermal fluctuations, surfaces are modeled based on heat conductance; moreover, conservation of energy is applied to model the interaction of surface and radiation.

The contribution of the paper is to introduce several physics-based models that are suitable for a variety of multisensor fusion problems. We provide guidelines on selecting the suitable models and parameters. In addition, we show how external and environmental sensory input are fused in a reasonable and unified manner.

3. PHYSICS-BASED MODELS

In the following we introduce physical models that describe the phenomenology of the visible and infrared part of the spectrum.

3.1 Reflectance Models (Visible)

There has been a number of physical models describing surface reflections. A complete treatment of all these models is beyond the scope of this paper; thus, we describe a few models that have been successfully applied both in computer vision and computer graphics to best model natural scenes. In order to proceed with the models, we first introduce the concept of lobes. In order to study surface reflections, first a framework for studying bidirectional reflectance distribution functions (BRDF) based on the concept of distribution of scattering light in

the form of lobes is introduced. Figure 1 describes the concept.

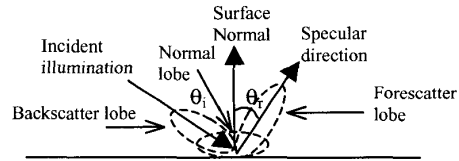


Figure 1. The lobe model describing BRDF.

The first model was introduced by Lambert and is known as Lambertian model which models the normal lobe. Simply stated, Lambertian model states that light scatters and reflects equally in all direction in the hemisphere above the incident light. The model is given as follows:

$$I = K I_{in} \cos(\theta_i) \quad (1)$$

where K is coefficient of reflection depending on surface material, I is the intensity observed, θ_i is the angle between incident illumination and the surface normal, and I_{in} is the intensity of the incident light and the BRDF is assumed to be: $f(\omega_i, \omega_r) = 1/\pi$ where ω_i, ω_r are solid angles subtending incident and reflected light. Although this model can approximate experimental data for a large set of materials, it is a poor approximation for rough surfaces.

An early attempt to model the forescatter lobe was made by Phong [12]. The model extends the Lambertian model and assumes maximum reflection along the perfect specular direction $\theta_i = \theta_r$, the model is given as:

$$I = K I_{in} \cos(\theta_i) + \cos^n(\alpha) \quad (2)$$

Where n describes the extend of spread of the forescatter lobe, and α is the angle between the viewing direction and the specular ray. Phong's model fails to account for Fresnel effects and assumes smooth surfaces, thus surfaces generated by this model are plastic and unnatural.

In the dichromatic reflection model [13], the backscatter and forescatter lobes are ignored and the specular component is assumed not to have been colored; therefore, the forescatter BRDF approximation is independent of the wavelength. In the dichromatic model, the reflection is based on two phenomenon, the interaction at the surface and the subsurface. Furthermore, reflection due to surface is assumed to be specular in nature and the surface of materials is assumed to have very few pigment particles; hence, the surface reflection component is unattenuated. The scattering and selective absorption due to pigments in the subsurface are what gives rise to the color of the surface. The dichromatic reflection model is described as:

$$\begin{aligned} L(\lambda, \theta_i, \theta_r) &= L_s(\lambda, \theta_i, \theta_r) + L_b(\lambda, \theta_i, \theta_r) \\ &= m_s(\theta_i, \theta_r) c_s(\lambda) + m_b(\theta_i, \theta_r) c_b(\lambda) \end{aligned} \quad (3)$$

where L is the total reflected intensity, L_i and L_b are reflected intensities due to surface and subsurface respectively, m_i and m_b are geometric terms and c_i and c_b are relative spectral power distribution (SPD) of the surface and subsurface respectively. The dichromatic model is useful in describing the reflection from inhomogeneous opaque dielectric materials (e.g., plastics). It is also useful in describing material colors since the SPD of the reflected light due to subsurface is decoupled from the geometric terms. Although the dichromatic model has been used in variety of computer vision tasks, it fails to model conductive materials which do not exhibit subsurface reflection and attenuate the wavelength of the interface reflection.

A more general model is given by Ward [14]. Depending on the level of sophistication required and the type of material desired to model, the Ward model can be extended to include diffuse, specular and colored reflections. The general Ward model is given as follows:

$$L(\lambda, \theta_i, \theta_r) = C \left[\frac{\rho_d}{\pi} + \rho_s \frac{1}{\sqrt{\cos(\theta_i) \cos(\theta_r)}} \frac{\exp(-\tan^2 \delta / \sigma_\alpha^2)}{4\pi\sigma_\alpha^2} \right] \quad (4)$$

where C is the material color vector which denotes the surface reflectance at three discrete wavelengths (R,G,B), ρ_d and ρ_s are diffuse and specular reflectance into the normal and foreshadow lobe respectively with the constraint that $\rho_d + \rho_s = 1$, σ_α is the rms slope and δ is the half angle as shown in Figure 2.

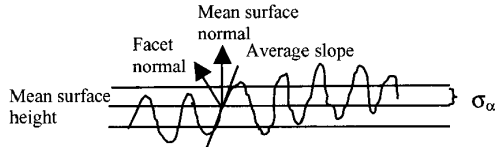


Figure 2. Facet and surface distribution model.

3.2 Thermal Models (Infrared)

Just as described in the previous section, there have also been a number of physical models proposed to model the thermal interactions in a scene. We describe physics that has been developed in different literatures for estimating heat fluxes. In the most general sense, heat fluxes can be viewed as the exchange of energy between molecules. A system of energy equilibrium describes these interactions based on three phenomenon: Energy Radiated (E_{rad}), Energy Conducted (E_{cd}), and Energy Convected (E_{cv}).

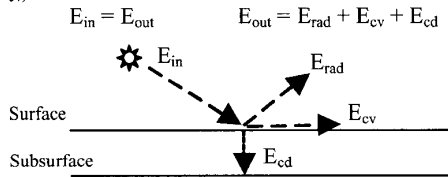


Figure 3. Conservation of energy and fluxes.

Figure 3 describes the conservation of energy, which states that the energy input to a system must equal to the energy output by a system.

In order to explain the above energies the following provides the basics of each phenomenon.

Radiation - Radiation is referred to as the energy emitted by matter that is of a finite temperature. Energy of a single quantum is given as: $E = h \nu$
 h = Planck's constant = 6.625×10^{-34}
 ν = frequency = c/λ ; c = speed of light, λ =wavelength
 Energy density of radiation per unit volume per unit wavelength is given by Planck's equation:

$$\eta_\lambda = \frac{8\pi h c \lambda^{-5}}{e^{\frac{hc}{\lambda k T}} - 1} \quad (5)$$

k = Stephan-Boltzman constant = 1.38066×10^{-23} J/molecule Kelvin, T = Temperature in Kelvin.

Integrating the above over all wavelengths, we'll have the famous Stephan-Boltzman law: $E_b = \sigma T^4$ (6)

where $\sigma = 5.669 \times 10^{-8}$ watts/m² Kelvin⁴ and the subscript b is for blackbody which is an idealized concept that refers to a body capable of 100% absorption (or emission) of energy. This law states that the energy radiated by a blackbody over all wavelengths is proportional to its internal temperature to the fourth power. The ramification of this law is that for a given blackbody temperature, its energy can be derived directly and vice-versa. Depending on the surface material, portion of radiation reaching a surface is absorbed, reflected and transmitted. Due to conservation of energy, these percentages must add up to 100%, that is:

$$\text{reflectivity } (\rho) + \text{absorptivity } (\alpha) + \text{transmissivity } (\tau) = 1 \quad (7)$$

Since most solids are opaque, their transmissivity is zero and $\rho + \alpha = 1$, or $\alpha = 1 - \rho$.

All bodies above absolute zero temperature emit energy in the form of radiation. Their ability to emit is referred to as emissivity or ϵ . For blackbodies, this emissivity is equivalent to absorptivity (α). For non-blackbodies, this value must be estimated. Emissivity of most materials generally varies with wavelength, temperature and surface conditions.

3.2.1 Models for E_{in}

In order to estimate the energy equilibrium, we must have an estimate of radiant energy that reaches the surface, E_{in} . The radiation reaching the earth's surface is a combination of complex interaction of sun's radiation with the environment. Some of these interactions involve the sky, the length of the path traversed (e.g. latitude, longitude), cloud cover, air quality, air pressure, air density, amount of water vapor and other particulates, and so on. The radiation reaching the earth's upper atmosphere is regarded as a constant and is given as approximately:

$$E_{\text{solar_const}} = 1089 \text{ W/m}^2 \quad (8)$$

Depending on the level of details and sophistication desired, any number of models can be applied to estimate E_{in} . In what follows we provide two models, the first one is based on individual atmospheric conditions, and the second one is based on lump atmospheric condition [16]. The models are provided as a set of equations.

Model 1

$$E_{\text{in}} = E_1 \tau_c \tau_a (\tau_{\text{atm}} - a_w)$$

$$\begin{aligned} E_1 &= E_{\text{solar_const}} \cos(Z); \\ Z &= \cos^{-1}[\sin(\text{lat}) \sin(\text{decl})] * [\cos(\text{lat}) \cos(\text{decl}) \cos(\text{Ha})]; \\ \text{decl} &= 0.006918 - (0.399912 * \cos(\text{FY})) + (0.070257 * \sin(\text{FY})) - \\ &(0.006758 * \cos(2*\text{FY})) + (0.000907 * \sin(2*\text{FY})) - (0.002697 * \\ &\cos(3*\text{FY})) + (0.00148 * \sin(3 * \text{FY})); \\ \text{FY} &= (2 * \pi / 365) * (\text{DayNum} + ((\text{Hour}-12)/24)); \\ \text{Ha} &= 15 * (12 - ((\text{LST} + ((4/60) * (\text{LSTM}-\text{long})) + (\text{EoT}/60))))); \\ \text{LST} &= \text{Hour} + \text{Minute}/60; \\ \text{EoT} &= 229.18 * (0.000075 + (0.001868 * \cos(\text{FY})) - (0.032077 * \\ &\sin(\text{FY})) - (0.014615 * \cos(2*\text{FY})) - (0.040849 * \sin(2*\text{FY}))); \\ \tau_c &= 1 - C_c (1 - C_i) \\ \tau_{\text{atm}} &= 1.021 - 0.0824 [(949 * B_{\text{kp}})/10^5 + (0.51/O_p)]^{1/2}; \\ O_p &= (O_m * B_{\text{kp}}) / 1013; \\ O_m &= 35 / [1224 * \cos^2(Z) + 1]^{1/2}; \\ a_w &= 0.077 [(P_w / O_p)]^{1/3}; \\ P_w &= [0.493 (H/100) e^{(26.23 - 5416/T_a)}] / T_a; \end{aligned}$$

Definitions for Model 1

E_1 = irradiation at the Earth's surface, τ_c = Cloud transmissivity, τ_a = Aerosol transmissivity (from look up table), τ_{atm} = atmospheric transmissivity, a_w = water vapor absorptivity, Z = Zenith angle, decl = Sun's declination angle, lat = Latitude, long = Longitude, FY = Fractional Year, Ha = Hour Angle, DayNum = Day Number (1..365) (e.g., Feb. 2 = 33), LST = Local Standard Time, LSTM = Local Standard Time Meridian (120° for Pacific Time), EoT = Equation of Time

C_c = Fraction of sky observed by cloud, C_i = Cloud type attenuation factor, B_{kp} = Atmospheric Pressure, O_p = Optical length, O_m = Optical Mass, P_w = Perceptible water, H = Relative humidity, T_a = Ambient Air Temp.

Model 2

$$\begin{aligned} E_{\text{in}} &= E_{\text{direct}} + E_{\text{skylight}} + E_{\text{atm}} \\ E_{\text{direct}} &= (1089.5/\text{ma}) e^{(-0.2819 \text{ ma})} \\ E_{\text{atm}} &= E(\text{BB}, T_a) \{1 - [0.261 e^{-7.77 * 10^{-4} (273-T_a)^2}]\} \end{aligned}$$

Definitions for Model 2

E_{direct} = direct irradiation due to sun
 E_{skylight} = irradiation due to sky $\approx (40-70 \text{ W/m}^2)$
 E_{atm} = irradiation due to upper atmosphere
 ma = The number of air masses ($\text{ma} \approx \secant(Z)$)
 T_a = Air temperature
 $E(\text{BB}, T_a)$ = radiation of a blackbody at T_a temp.

3.2.2 Models for E_{cv}

The convective heat flux is due to transfer of heat by the motion of fluids. The heat flux at the surface is given by:

$$E_{\text{cv}} = h (T_s - T_\infty) \quad (9)$$

where h is the coefficient of convection that depends on many factors. Although there exist two types of convections *free convection* (due to buoyancy of materials) and

forced convection (due to fluid flow), we only consider the forced convection since the effect of free convection can be negligible in many circumstances. The forced convection can be *laminar* or *turbulent* depending mainly on the fluid velocity. The coefficient of convection depends on what type of fluid flow is considered.

The most important parameter in estimating the convective heat flux is h . Derivation of h is complex for general scene; however, it can be estimated for flat plates as follows. First the Reynold number is decided. Depending on the value of the Reynold number, correct equation for the Nusselt number for a particular surface geometry and flow condition is used. Finally, the Prendt number is calculated to derive the Nusselt number hence the coefficient of convection, h . The process is given as follows:

$$\text{Re} = (\mu_\infty x) / \nu \quad (10)$$

μ_∞ = Free stream velocity; x = distance from the edge ; ν = kinematic viscosity.

If $\text{Re} \geq 5 * 10^5$ then flow condition is considered to be turbulent. In addition to the flow condition, the equation for the Nusselt number depends on the surface geometry. For a flat plate the Nusselt number is given as follows [15]:

$$\begin{aligned} \text{Laminar (11)} & \quad \text{Turbulent (12)} \quad \text{Mixed (13)} \\ 0.664 \text{Re}^{1/2} \text{Pr}^{1/3} & \quad 0.0592 \text{Re}^{4/5} \text{Pr}^{1/3} \quad (0.037 \text{Re}^{4/5} - 871) \text{Pr}^{1/3} \end{aligned}$$

where the Pr is the Prendt number:

$$\text{Pr} = C_p \mu / k_f; \quad (14)$$

$$h = (k_f \text{Nu}) / L; \quad (15)$$

C_p = fluid specific heat, and μ = dynamic viscosity, k_f = fluid conductivity, L = characteristic length, Nu = Nusselt. A back of the envelop, simpler estimation of h is given in [15]:

$$h = 1.7 [T - T_a]^{1/3} + (6 \text{Va}^{0.8}) / L^{0.2} \quad (16)$$

Va = wind speed; L = characteristic Lateral dimension of surface.

3.2.3 Models for E_{cd}

To complete our thermal model, we now consider the heat flux due to conduction. Conduction is the energy transferred through molecular interaction when a gradient temperature exists. As shown in Figure 4, the energy due to heat flow per unit time is:

$$(Q/t) = [k A (T_2 - T_1)] / L \quad (17)$$

The quantity to the left is the energy transfer due to conduction E_{cd} . It is also customary to divide both the numerator and denominator of the right side of this equation by k so:

$$E_{\text{cd}} = A (T_2 - T_1) / (L / k) \quad (18)$$

where L/k is called the thermal resistance or R-value and is tabulated for many materials.

Thermal conductivity is also expressed in terms of thermal diffusivity. Thermal diffusivity measures the ability of material to conduct thermal energy relative to its ability to store thermal energy and is given as:

$$d_\alpha = k / [D_p C_p]; \quad (19)$$

D_p = density, C_p = Specific Heat = $(Q / m(T_2 - T_1))$, m = mass. Materials with small d_α respond quickly to environment; whereas, materials with large d_α take longer to reach equilibrium. Another approximation for conductive heat flux is also given as:

$$k(T - T_0) = 2 C_p h_d D (dT_0 / dt) \quad (20)$$

where D = Density, h_d = effective thermal depth of heat storage, dT_0 = change in interior temperature, dt = short time interval allowed for temperature change.

An estimation for h_d is given as:

$$h_d = [2k / (2\pi C_p D)]^{1/2} \quad (21)$$

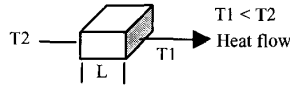


Figure 4. Heat flow in a flat plate. k = conductive coefficient, A = Area, L = Length, T_1, T_2 = temp.

The method in (20) requires knowledge of the initial value for the interior temperature. Since this is not possible, an initial value can be estimated based on the diurnal temperature for the current season and through an iterative process, as more values are measured, a more accurate estimate of this value can be achieved.

4. EXPERIMENTAL RESULTS

4.1 Reflectance Model

The data was collected (see Figure 5) by a 3CCD, SONY DCR1000 digital camera equipped with a dichroic prism splitting the light into three R, G, B channels. The dichromatic reflection model (3) is used to estimate the color and reflectance properties of the typical outdoor surfaces under natural illumination. We use an algorithm based on spatio-temporal albedo segmentation and singular value decomposition to calculate the normalized colors in the dichromatic space [11]. Figure 5 indicates several examples with areas chosen to indicate the subsurface (or body) color of the patches in the scene.

In order to calculate the color vector (C_b), we first select and arrange pixels on a surface as follows:

$$C = \begin{bmatrix} R_1 & G_1 & B_1 \\ R_2 & G_2 & B_2 \\ \vdots & \vdots & \vdots \\ R_m & G_m & B_m \end{bmatrix} \quad (22) \quad \text{and} \quad C = U \Sigma V^T \quad (23)$$

where C is an $m \times 3$ real matrix. For $m \geq 3$, matrix C can be factorized as in (23), where U and V are orthogonal square matrices, $\Sigma = \text{diag}(\sigma_1, \sigma_2, \sigma_3)$ with $\sigma_1 \geq \sigma_2 \geq \sigma_3 \geq 0$ and superscript T represents the transpose operation. A standard singular value decomposition (SVD) method is then applied to matrix C which yields matrices, U , Σ , and V , where Σ represents eigenvalues in descending order corresponding to eigenvector columns of matrix

V^T . We have shown that the principal component vector (vector corresponding to the largest eigenvalue) aligns naturally with C_b [11]. Furthermore, eigenvalues ($\sigma_1, \sigma_2, \sigma_3$) provide an error term where we should expect ($\sigma_1 \gg \sigma_2$).

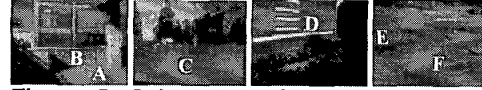


Figure 5. Selected background frames representing surfaces at different locations. A=Concrete (flat), B=Red Brick (textured), C=Grass (curved), D=Red Tile, E=Grass, F=Concrete (textured).

The dichromatic reflection model was used on the areas shown in Figure 5, to estimate the surface colors. The following table indicates the body color vector (C_b) for each surface generated by our algorithm. These vectors are normalized in the unit RGB space.

Surface	C_b		
	R	G	B
A	0.6110125	0.620583	0.491460
B	0.6712749	0.596953	0.436713
C	0.6407066	0.692914	0.307031
D	0.6795831	0.545452	0.456399
E	0.6377073	0.683179	0.309178
F	0.6539630	0.608791	0.449115

Because of the sensitivity of the color matching and normalization, the results are reported with 6 significant digits. As can be seen surfaces such as grass (surfaces C and E) with similar characteristics, aligned closely in the dichromatic plane. Subtle differences in texture and types of mixed materials can also influence the reflection properties, for example, surfaces A and F both are concrete yet their body color differs significantly. This is also clear from Figure 5 where surface A is more uniform whereas surface F is more textured. On the other hand, surfaces such as B (red-brick) and D (red-tile) with similar color properties in one channel (e.g., red), may still be distinguished from each other in the dichromatic space due to their subsurface properties.

4.2 Thermal Model

We have utilized a FLIR SC2000 long wave infrared camera to measure and record surface temperatures based on radiation fluxes. The thermal equilibrium model is then utilized to estimate the surface temperatures separately. The data was collected in southern California at location with latitude $33^\circ 55' 39''$ N and longitude $117^\circ 21' 17''$ W, between 3:30 p.m. – 10:30 a.m. on march 10-11, 2002. Ambient air temperature, and wind velocity were user specified based on reported weather.

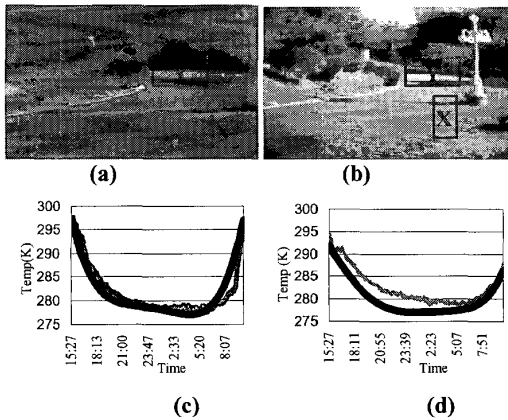


Figure 6. Graphs showing thermal measurements of two types of surfaces and the predicted values by the physical models. Solid black lines indicate predicted values and colored lines show the actual measurements. (a) Thermal image, (b) Video image, (c) area X (grass/dirt), (d) area Y (Cement/Concrete).

In addition to the energy equilibrium model of section 3.2, we utilized model 1 for E_{in} , and equations (9), and (18) where fluid flow was considered laminar (11), and the R-value in (18) was user specified for the particular material. For the grass and concrete an average conductivity of 1.2 and 0.8 W/mK was used respectively. Surface emissivity of concrete was fixed at 0.92 and for grass area at 0.97. Thermal measurements were performed at intervals of 1.5 minutes. Other parameter values such as ambient temperature and wind velocities were input to the system by the available weather data. As shown, the grass area was predicted much closer than the cement area. The fluctuations and differences are due to the complex surrounding structures and natural objects. These objects also create shadows on surfaces at different times of the day. We were able to track the major changes in the temperatures, for example, the slope of the lines are tracked closely. In Figure 7 (d), the properties of the exact surface material such as its type, surface condition and the material below the surface was not available. This information, in addition to real environmental conditions at the location, can further help to predict the temperatures more accurately.

5. CONCLUSIONS

Physics-based sensor fusion provides a natural way of integrating sensors and external conditions in a unified manner. We have provided several physical models for the visible and thermal ranges of the spectrum. We have also shown the strength and weaknesses of each of these models in order of increasing sophistications and provided guidelines for applicability of each of the models.

In addition, we have shown examples of these models applied to real world surfaces. The more sophisticated models require a number of variables that need to be input to the system. This increases accuracy at the expense of computational complexity. There is a trade-off of the model complexity vs. accuracy and computational overhead. Application specifics determine the appropriate values in practice.

Acknowledgement – This work was supported in part by grant F49620-02-1-0315 and DAAD19-01-0357; the contents and information do not necessarily reflect the position or policy of U.S. Government.

References

- [1] D.L. Hall, and J. Llinas, "An introduction to multisensor fusion", *Proc. of the IEEE*, Vol. 85, No. 1, pp. 6-25, Jan. 1995.
- [2] B.V. Dasarathy, "Fusion strategies for enhancing decision reliability in multisensor environments", *Optical Engineering*, Vol. 35, No. 3, pp. 603-616, Mar. 1996.
- [3] S. Nadimi and B. Bhanu, "Multistrategy fusion using mixture model for moving object detection," *Proc. Intl. Conf. on Multisensor Fusion and Integration for Intelligent Systems*, pp. 317-322, Aug. 2001.
- [4] D. M. Buede, and P. Girardi, "A target identification comparison of Bayesian and Dempster-Shafer multisensor fusion", *IEEE Transactions on Systems Man & Cybernetics*, Vol. 27, No. 5, pp. 569-577, Sept. 1997.
- [5] H. Zhang, "Multisensor data fusion by improved Hough transformation", *High Technology Letters*, pp.7-11, Dec. 1995.
- [6] M.E. Ulug, and C. McCullough, "Feature and data level fusion of infrared and visual images", *Proc. SPIE: Intl. Society for Optical Engineering*, Vol. 37, No. 19, pp. 312-318, Apr. 1999.
- [7] C.W. Therrien, J.W. Scrofani, and W.K. Krebs, "An adaptive technique for the enhanced fusion of low light visible with uncooled thermal infrared imagery", *Proc. Intl. Conf. on Image Processing*, Vol. 3, pp. 405-409, 1997.
- [8] N. Nandhakumar, and J.K. Aggrawal, "Physics-based integration of multiple sensing modalities for scene interpretation", *Proc. of the IEEE*, Vol. 85, No. 1, pp 147-163, Jan. 1997.
- [9] D. Terzopoulos, and D. Metaxas, "Dynamic 3D models with local and global deformations: deformable superquadrics", *IEEE Transactions on Pattern Analysis & Machine Intelligence*, Vol. 13, No. 7, pp. 703-714, July 1991.
- [10] I. Pavlidis, et. al. "Automatic detection of vehicle passengers through near-infrared fusion", *Proc. IEEE Conf. on Intelligent Transportation Systems*, pp. 304-309, Oct. 1999.
- [11] S. Nadimi, B. Bhanu, "Moving shadow detection using a physics-based approach," *IEEE Intl. Conf. on Pattern Recognition*, pp. 701-704, Aug. 2002.
- [12] B.T. Phong, "Illumination for computer generated pictures," *Communication of the ACM*, Vol. 98, No. 6, 1975.
- [13] S. A. Shafer, "Using color to separate reflection components", *COLOR Research and Application*, Vol. 10, No. 4, pp. 210-218, 1985.
- [14] G. Ward, "The RADIANCE lighting simulation and rendering system", *Computer Graphics (SIGGRAPH' 94)*, pp. 459-472, July 1994.
- [15] F.P. Incorpera, and D.P. DeWitt, Introduction to Heat Transfer, John Wiley & Sons, 1990.
- [16] G. Zissis, The Infrared & Electro-Optical Systems Handbook, Volume 1, SPIE Optical Engineering Press, 1993.